Lab on a Chip

A numerical lift force analysis on the inertial migration of a deformable droplet in steady and oscillatory microchannel flows

Journal:	*Lab on a Chip*
Manuscript ID	LC-ART-02-2022-000151.R3
Article Type:	Paper
Date Submitted by the Author:	27-Jun-2022
Complete List of Authors:	Lafzi, Ali; Purdue University System, Agricultural and Biological Engineering Dabiri, Sadegh; Purdue University System,

A numerical lift force analysis on the inertial migration of a deformable droplet in steady and oscillatory microchannel flows

Ali Lafzi[1] and Sadegh Dabiri[1,2]

[1]*Department of Agricultural and Biological Engineering, Purdue University, West Lafayette, Indiana 47907, USA*

[2]*School of Mechanical Engineering, Purdue University, West Lafayette, Indiana 47907, USA*

Abstract

Inertial migration of deformable particles has become appealing in recent years due to its numerous applications in microfluidics and biomedicine. The physics underlying the motion of these particles is contingent upon the presence of lift forces in microchannels. Therefore, in this work, we present a lift force analysis for such migration of a deformable droplet in steady and oscillatory flow regimes and identify the effects of varying Capillary number and oscillation frequency on its dynamics. We then propose an expression that mimics the lift force behavior in oscillatory flows accurately. Finally, we introduce a procedure to derive and predict a simple expression for the steady and averaged oscillatory lift for any given combination of Capillary number and oscillation frequency within a continuous range.

I. INTRODUCTION

Inertial migration of particles in microchannels has caught extensive attention in the last two decades due to its numerous applications in cell sorting, fractionation, filtration, and separation in many clinical practices [1–4]. The presence of lift forces acting on these particles is the chief reason for observing the underlying physical phenomena in microfluidic systems [5–9]. The importance of these forces has motivated many researchers to analyze or measure them within the microchannel. *Di Carlo et al.* have derived the inertial lift on particles and studied the effects of channel Reynolds number and particle size on it; they have shown that by increasing Reynolds, the magnitude of lift coefficient decreases near the wall and increases near the channel center [10]. Also, the particle equilibrium positions shift toward the center as its size increases and its rotational motion is not a key component of the inertial lift. Using lift force profiles, *Prohm and Stark* have investigated and categorized the particle focusing points and demonstrated that the stable fix points lie on either the diagonal or main axes of the channel cross-section [11]. *Su et al.* have proposed a fast numerical algorithm combined with machine learning techniques to predict the inertial lift distribution acting on solid particles over a wide range of operating parameters in straight microchannels with three types of geometries by specifying the cross-sectional shape, Reynolds number, and particle size [12].

Furthermore, there have been attempts to derive analytical relationships for the observed behaviors. A simple formula using data fitting and least square was obtained to investigate the relationship between the lift and particle size and Reynolds number; according to the proposed criterion, particle focusing does not occur for too small particles or too low Reynolds numbers [13]. *Asmolov et al.* illustrated that the velocity of finite-size particles near the channel wall is different from that in the undisturbed flow and then reported a generalized expression for the lift force at $\mathrm{Re} \leq 20$ [14]. Another study has proposed a generalized formula for the inertial lift acting on a sphere that consists of 4 terms: wall-induced lift, shear-gradient-induced lift, slip-shear lift, and correction of the shear-gradient lift; the authors have further confirmed that wall and shear-gradient are the main features of the lift [15]. Moreover, there are examples of works concentrating on the effect of particle shape. For instance, *Zastawny et al.* presented the great influence of shape both by changing the experienced values of forces and torques and modifying the Reynolds at which the transition

to unsteady flow happens [16]. Further extension on previous theories and analytical works resulted in an analytical expression capturing the weak, inertial lift on an arbitrarily-shaped particle moving near a wall [17].

Most of the studies on lift forces in the microchannels have focused on solid particles or non-deformable objects and have analyzed the effect of parameters such as channel Reynolds, particle size, etc. Therefore, there are very few examples presenting the whole lift force profiles acting on deformable particles such as droplets and bubbles and studying the effect of their corresponding parameters like Capillary number on the force values. For example, *Chen et al.* have extensively studied the inertial migration of a deformable droplet in a rectangular microchannel, but their presented lift force profile only considers one value for particle Weber number (a measure for particle deformability) [18]. *Rivero-Rodriguez and Scheid* have divided the underlying physics into different regimes. In the pure inertial regime, they have plotted the inertial lift on a rigid bubble at different Reynolds numbers, and in the pure Capillary regime where the inertial effects are absent, a lift profile is presented for different Capillary numbers [19]. However, their work lacks a similar profile visualizing the total lift force in the most general nonlinear inertial-capillary regime.

The obtained lift force profiles are mainly the result of either some experimental measurements [10, 20, 21] or applying a feedback control in the numerical code to fix the position of particle [22], capsule [23], or drop [18]. Nevertheless, in this paper, we present a method for lift force calculation at different Capillary numbers that solely depends on the trajectory of the drop. In addition, the importance of exploiting an oscillatory flow in the microchannel for working with sub-micron particles [24], having direct control over their focal points and tuning them depending on the flow oscillation frequency [25], and more effective separation and sorting strategies [26] has already been presented in the literature. Thus, we will expand our lift force analysis to include both steady and oscillatory regimes at various Capillary numbers, where the latter is completely missing in the literature. We will then try to fit analytical expressions to the obtained lift profiles for different cases and present a scheme to predict this expression over a continuous range of input parameters.

II. METHODOLOGY

A single droplet with density and viscosity ratios of one is placed in a laminar flow of an incompressible Newtonian fluid in a microchannel as illustrated in Fig. 1. The drop dynamics is simulated using the Front-tracking method [27]. In this approach, the governing equations are solved in the fixed Eulerian grid, and the obtained flow field information is used to update the properties across the droplet surface, which is tracked in a Lagrangian manner. The governing equations to be solved in the entire computational domain are the continuity and momentum equations:

$$\frac{\partial \rho}{\partial t} + \nabla \cdot (\rho \mathbf{u}) = 0, \tag{1}$$

$$\frac{\partial (\rho \mathbf{u})}{\partial t} + \nabla \cdot (\rho \mathbf{u}\mathbf{u}) = -\nabla P + \nabla \cdot \left[\mu(\nabla \mathbf{u} + \nabla \mathbf{u}^T)\right] + \iint \gamma \kappa \delta(\boldsymbol{x} - \boldsymbol{x_i}) \mathbf{n} dA, \tag{2}$$

where ρ is the density of the fluid, P represents the pressure, $\mathbf{u}$ is the flow velocity vector, t is the time, μ is the fluid dynamic viscosity, κ is the curvature at the interface, γ is the surface tension, δ is the Dirac delta function, $\boldsymbol{x}$ is an arbitrary location in the computational domain, $\boldsymbol{x_i}$ is such position on the drop interface, and $\mathbf{n}$ is the unit normal vector to a point on the drop interface. The aforementioned delta function is defined as:

$$\delta(x) = \tilde{D}(x)\tilde{D}(y)\tilde{D}(z), \tag{3}$$

$$\tilde{D}(x) = \frac{1}{4\Delta}(1 + \cos(\frac{\pi}{2\Delta}(x))), |x| \leq 2\Delta, \tag{4}$$

where Δ is the Eulerian grid length.

The pressure gradient in the x direction has a constant magnitude of P_0 for the steady flow and a varying strength of $P_0 cos(\omega t)$ for the oscillatory flow. The periodic boundary condition is applied in the x direction, and the no-slip condition is applied on the walls in the y and z directions. Parameters W and U_c (maximum velocity of the steady case) are used as the characteristic length and velocity, respectively. In other words, $x^* = \frac{x}{W}$, $u^* = \frac{u}{U_c}$, $t^* = \frac{t}{\frac{W}{U_c}}$, $P^* = \frac{P}{\mu \frac{U_c}{W}}$, $T^* = \frac{T}{\frac{W}{U_c}}$ (where T is the period), and $\omega^* = \frac{2\pi}{T^*}$. Three dimensionless parameters describe the dynamics of the drop: (i) Reynolds number, $Re = \frac{\rho U_c 2W}{\mu}$, (ii)

Capillary number, $Ca = \frac{\mu U_c}{\gamma}$, and (iii) the dimensionless oscillation frequency (ω^*). The drop has a constant size of $\frac{a}{W} = 0.3$ with a spherical initial shape, and $Re = 10$ in our entire study. The numerical grid is generated using $196 \times 114 \times 114$ cells in the x, y, and z directions, respectively, and with 29578 triangular elements for the discretization of the drop interface.

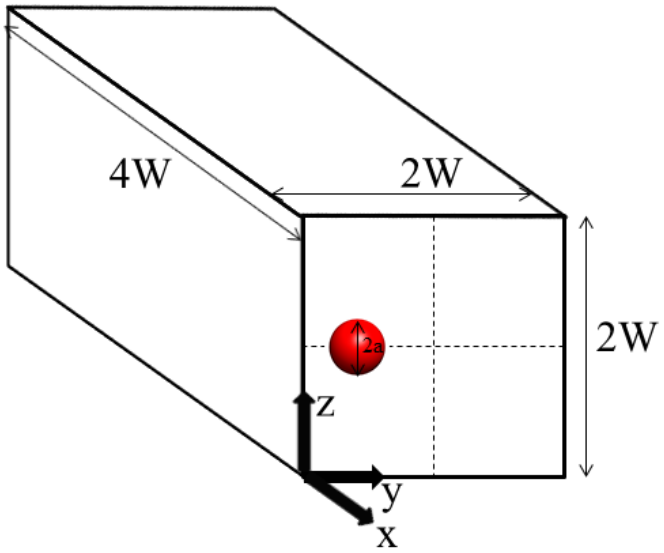

FIG. 1: Schematic of the problem setup

The droplet Lagrangian equation of motion has the following form [15, 28]:

$$m_d \frac{d\mathbf{U}_d}{dt} = \sum \mathbf{F} + C_{am}\rho V_d\left(\frac{D\mathbf{u}}{Dt} - \frac{d\mathbf{U}_d}{dt}\right), \tag{5}$$

Where m_d is the mass of the drop, $\mathbf{U}_d$ is its velocity, $\sum \mathbf{F}$ is the sum of all other force terms acting on the droplet, including gravity, pressure gradient, drag, lift, Basset, etc. The second term on the right-hand side is the added mass effect in which, C_{am} is the coefficient of added mass, and V_d is the volume of the droplet (or the displaced volume of the fluid). The coefficient C_{am} can be calculated using the following formula [29, 30]:

$$C_{am} = \frac{\sqrt{\chi^2 - 1} - cos^{-1}(\frac{1}{\chi})}{cos^{-1}(\frac{1}{\chi}) - \frac{\sqrt{\chi^2-1}}{\chi^2}}, \tag{6}$$

In which, χ is the aspect ratio of the drop.

The main focus of this work is on the cross-stream migration of the droplet. As we know,

the pressure gradient in the wall-normal direction is zero. Furthermore, in this direction, the fluid velocity ($\mathbf{u}$) is negligible compared to that of the droplet ($\mathbf{U}_d$), and the droplet velocity is its migration velocity. Also, because the density ratio is one, the droplet is neutrally-buoyant. In other words, the effective gravitational force can be neglected in this case [15, 28]. Moreover, since the droplet acceleration rate is not high, the Basset history force is much smaller than the drag force and can be neglected. Consequently, for the wall-normal direction, equation 5 can be re-written as:

$$m_d(1 + C_{am})\frac{dv_r}{dt} = \mathbf{F}_{lift} + \mathbf{F}_{drag}, \tag{7}$$

Where v_r is the droplet migration velocity.

There are certain types of drag and lift forces that act on the drop as it travels its lateral trajectory in the wall-normal direction across the channel. Accounting for the fact that Magnus and Saffman lift forces are often the negligible components, the active dominant forces on the migrating drop in the wall-normal direction are the lateral drag and inertial and deformation-induced lift forces [6, 9, 31, 32]. The inertial lift consists of two components:

1. **The wall effect**: The channel wall retards the particle motion by creating translational and rotational differences between its velocity and that of the surrounding fluid. This occurs due to the uneven formation of vortices around the particle that pushes it toward the channel center [31, 33, 34].

2. **The shear gradient lift**: The curvature in the shape of the fluid velocity profile makes the magnitude of the relative velocity of the fluid with respect to the particle to be higher on the wall side compared to that of the channel center side. This magnitude difference induces a low pressure on the wall side leading to the formation of a shear gradient lift that repels the particle toward the wall [31].

The deformation lift pushes the deformable droplet towards the channel center to minimize its surface energy [19, 31, 32, 35]. The direction of the lateral drag is the opposite of the drop migration velocity, assuming that the carrier fluid is stationary in the wall-normal direction. Therefore, if we assume the positive direction to be from the channel center to the wall, the force balance on the drop (eq. 7) in the wall-normal direction is the following:

$$F_{total} = F_{inertial} - F_{deformation} - F_{drag}, \tag{8}$$

Assuming a density ratio of one between the fluids inside and outside of the drop, the above equation can be rewritten as:

$$m_d(1 + C_{am})a_r = (F_{shear\,gradient} - F_{wall}) - F_{deformation} - F_{drag}, \tag{9}$$

Where a_r is the migration acceleration of the drop. Since the droplet in this study has large distances from the wall, the wall effect is negligible compared to the shear gradient force in the inertial lift [31, 33, 36]. Also, to the best of our knowledge, there is no analytical equation for the shear gradient lift in the literature to date.

The drag force is computed based on its physical definition [37]:

$$F_{drag} = \frac{1}{2} C_D \rho v_r |v_r| A_d, \tag{10}$$

$$C_D = \frac{24}{Re_{rel}}(1 + 0.1 Re_{rel}^{0.75}), \tag{11}$$

$$Re_{rel} = Re \frac{v_r}{U_c} \frac{a}{W}, \tag{12}$$

Where C_D is the drag coefficient, v_r is the relative velocity between the drop and the fluid in the lateral direction (which is essentially its migration velocity), and A_d is the frontal projected area of the drop. Equation 11 is consistent with the findings of [37–41] and those of [42] at a viscosity ratio of one. Although eq. 11 is derived for steady flows, researchers have shown that the drag coefficient in unsteady flows depends heavily on an unsteady parameter that includes the density ratio [43, 44]. Since the density ratio in the present study is one, the aforementioned unsteady parameter becomes zero, and hence, C_D for unsteady flows (including oscillatory cases) can be approximated as the one for steady flows using this equation. The parameter A_d is calculated based on the projected area of the drop on a plane having a normal vector parallel to its migration velocity. Thus, the value of this parameter varies at different instances. This procedure leads to a more precise computation of the drag force.

Considering a viscosity ratio of one, the deformation-induced lift for a drop that has a distance higher than its diameter from the closest wall leads to the following compact form

[45, 46]:

$$F_{deformation} = 75.4 Ca_p \mu V_{avg} a (\frac{a}{W})^2 \frac{d}{W}, \tag{13}$$

Where $Ca_p = Ca\frac{a}{W}$ is the drop capillary number, V_{avg} is the average velocity of the carrier fluid across the channel, and d is the distance of the drop from the channel center. The linear dependency of this force with respect to the distance d in the specified region is also confirmed in [19].

The lift force analysis in this work is solely based on the drop trajectory. Therefore, to get a lift profile that spans a wide range of d, the drop is released from two different initial locations:

- $y^* = 0.46$ and $z^* = 1$ (the upper release)
- $y^* = 0.98$ and $z^* = 1$ (the lower release)

The upper release is chosen such that the whole range of studied d falls within the validity domain of the deformation force equation (eq. 13). This enables us to plug eq. 13 into the force balance equation (eq. 8) to get the inertial force once the total force is calculated as elaborated below. We will compare the inertial force at different Ca values for the steady flows in the results section. The lower release initial location is slightly off from the channel center since it is also an equilibrium point, and if a drop is placed there, it does not move at all [18]. The initial z component for both releases is on the main axis for faster convergence since the drop eventually focuses on the main axes according to our previous work [47]. These different initial locations do not alter the drop equilibrium position [48–51]. The results of each parameter computation for both releases will be combined to reflect its overall behavior within the channel cross-section.

The migration velocity and acceleration of the drop is calculated by taking the first and second temporal derivatives from its trajectory numerically. Since time-step varies throughout the simulations to keep the Courant–Friedrichs–Lewy (CFL) number at 0.9, the following equations are used to obtain the corresponding derivatives [52]:

$$v_r = \dot{d_i} \approx \frac{-h_i}{(h_{i-1})(h_i + h_{i-1})} d_{i-1} + \frac{h_i - h_{i-1}}{h_i h_{i-1}} d_i + \frac{h_{i-1}}{(h_i)(h_i + h_{i-1})} d_{i+1}, \tag{14}$$

$$a_r = \frac{dv_r}{dt} = \ddot{d}_i \approx \frac{2\left[d_{i+1} + \frac{h_i}{h_{i-1}}d_{i-1} - (1 + \frac{h_i}{h_{i-1}}d_i)\right]}{h_i h_{i-1}(1 + \frac{h_i}{h_{i-1}})}, \tag{15}$$

In which $h_i = t_{i+1} - t_i$, $h_{i-1} = t_i - t_{i-1}$, and d_i and t_i denote the distance from center and time at the current step, respectively. Both non-uniform finite difference schemes have a second-order accuracy.

Taking the first derivative from the steady flow trajectory at the lowest Ca ($Ca = 0.09$) results in a very noisy curve that is impossible to interpret. Therefore, we use an accurate non-linear regression by minimizing the sum of squared errors to fit the trajectories with analytical expressions, from which we can take first and second derivatives analytically. The trajectory from the upper release is very similar to an exponential decay. Therefore, we fit a curve with the following form to it:

$$d(t) \approx ce^{bt} + k, \tag{16}$$

Where c, b, and k are all constants that should be determined by curve fitting. The constant k is essentially the drop equilibrium distance from the center. The trajectory from the lower release looks like the sigmoid logistic function. Consequently, we use the following equation as its analytical general form:

$$d(t) \approx \frac{c}{1 + e^{-b(t-k)}} + offset, \tag{17}$$

Where again, c, b, k, and $offset$ are the regressor constants. The regression fits to both trajectories from the upper and lower release have very high R^2 scores of 0.99 as plotted in fig. 2. This figure further confirms that the drop focuses at the same d^* regardless of its initial location.

Once the migration acceleration is derived following the aforementioned steps, it will be multiplied by the effective mass of the drop, as pointed out in eq. 9, to calculate the total force on the left-hand side of this equation. The term m_d in this equation is equal to $\frac{4}{3}\pi a^3 \rho$, which is the total constant mass of the drop with the initial spherical shape. The exact computation of the added mass coefficient requires separate extensive work. Therefore, as a zeroth-order approximation, the term (C_{am}) in eq. 9 is considered to be 0.5, which is the value for a solid spherical particle. *Salibindla et al.* have shown that the added mass

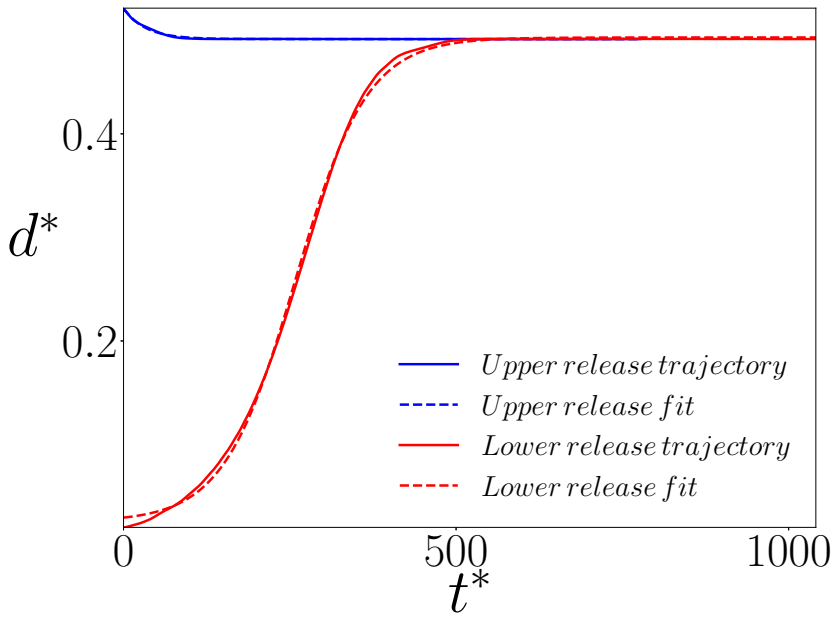

FIG. 2: Regression fits to both steady trajectories at $Ca = 0.09$

coefficient for deformable bubbles decreases as the bubbles deform and their aspect ratio along their semi-major and minor axes increases [53]. *Sangani et al* have illustrated that the changes in the added mass of the bubbles as a function of their surface tension (or Capillary number) are very small and negligible [54]. *Presas et al.* have also mentioned that the added mass generally increases as the surface of the particle becomes more rigid [55]. These findings imply that the added mass coefficient for a non-deformable particle is the maximum. Furthermore, after completing the calculations, it turns out that the left-hand side of eq. 9 is much smaller than the calculated drag force on the right-hand side. Consequently, this observation combined with the findings and reports of the aforementioned studies confirms that the more exact calculation of the added mass does not change the analysis and results significantly compared to the presented ones with the upper-bound approximation used for C_{am} in our work. Finally, by subtracting the drag force from the total force, the total lift force can be obtained.

III. RESULTS AND DISCUSSION

In this section, we report the results of a single deformable droplet simulations in the previously introduced microchannel that contains either steady or oscillatory carrier fluid.

As we are interested in studying the effects of oscillation frequency and Capillary number on the lift force, we fix the Re at a value of 10. Ca ranges between 0.09 and 1.67, and for oscillatory cases, ω^* values are chosen such that for a channel with a cross-section of $100\mu m$ and water as the working fluid at room temperature, the frequency ranges between 2Hz and 200Hz, which is mostly referred to in the literature [56].

As mentioned earlier in the introduction, to the best of our knowledge, the literature is missing a comprehensive and complete lift force analysis, taking all its dominant components into account, or a migration velocity analysis versus distance from the channel center for the case of deformable droplets or bubbles in the microchannel flows with a square channel cross-section. Also, as we will see in the following sections of the paper, the inertial lift turns out to be a function of Ca, and hence, we cannot compare it to those of other works performed for solid or non-deformable particles for validation purposes. Therefore, since our scheme is based on the droplet trajectory, which depends on inertial and deformation effects, we have compared our numerical results from these effects to the corresponding ones of other works for validation. For instance, the drop deformations at $Ca = 0.2$ and different Deborah numbers are compared with those of *Aggarwal and Sarkar* [57] and are in good agreement with theirs having a maximum error of 0.72%. The droplet trajectories at $Re = 8.25$, $Ca = 0.18$, $\frac{a}{W} = 0.2$ and $Re = 21$, $Ca = 0.14$, $\frac{a}{W} = 0.3$ have been compared with those reported by *Marson et al.* [58], where our results lie within their uncertainty bands. Furthermore, we have shown that the numerical results are independent of the distance between two consecutive drops in an infinite domain in the flow direction. This has been done by comparing the drop trajectory at $Re = 10$, $Ca = 1$, and $\omega^* = 0.1$ for three different channel lengths of $4W$, $6W$, and $8W$ in our simulations. The maximum difference between the drop trajectories for $L = 4W$ and $L = 6W$ is $0.0003W$ (0.1%), and the one between those of $L = 4W$ and $L = 8W$ is $0.0005W$ (0.2%). The results have also been shown to be mesh independent by comparing the drop trajectories for the case of $Re = 10$, $Ca = 1$, and $\omega^* = 0.1$ with two different grids of $196 \times 114 \times 114$ and $256 \times 152 \times 152$. The maximum difference between their drop distances from the channel center is $0.0009W$ (0.3%). More detail can also be found in our previous work [47].

Figure 3 illustrates the dimensionless average velocity of flow across the channel over dimensionless time. It can be seen that while the steady regime has the largest constant V^*_{avg} in a single direction, the average of oscillatory V^*_{avg} in each half of a periodic cycle

decreases by increasing the frequency [25, 47]. Although the average of a sinusoidal function in half of a period is constant regardless of its oscillation frequency ($\frac{1}{\frac{\pi}{\omega}} \int_0^{\frac{\pi}{\omega}} sin(\omega t)dt = \frac{2}{\pi}$), the lower maximum absolute value of V^*_{avg} at higher frequencies is the chief reason for the observed phenomenon.

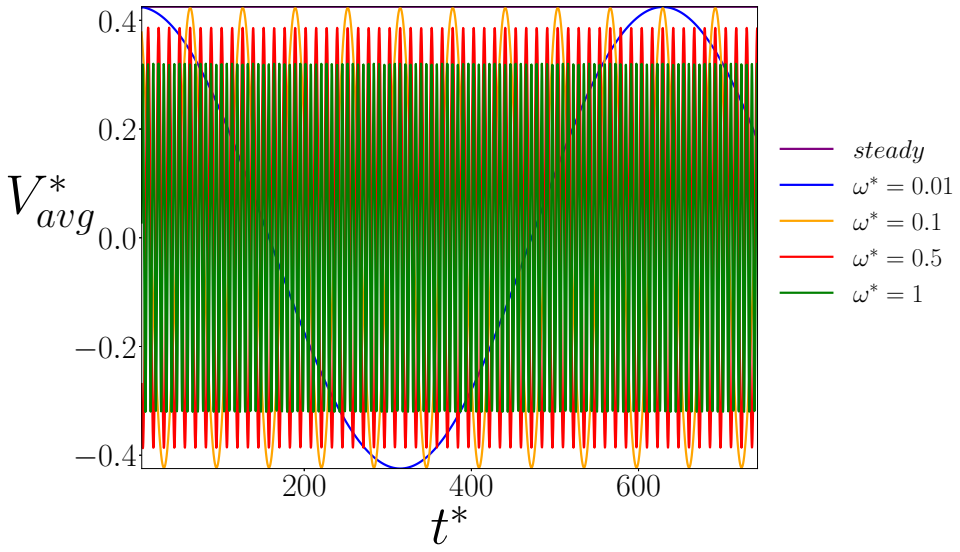

FIG. 3: Average velocity of flow across channel cross section versus time at $Ca = 1.67$ and $Re = 10$

Figure 4 visualizes the dimensionless time-dependent frontal projected area of the droplet (parameter A_d in equation 10) as it migrates toward its lateral equilibrium position traveling both upper and lower-release trajectories. The first thing we note is that in the transient stage before focusing, the drop has a higher average projected area while traveling the upper trajectories (fig. 4b) compared to the one in the lower trajectories (fig. 4a) in each of the flow regimes correspondingly. This is because the drop experiences more shear and deforms easier when traveling the upper trajectories. Moreover, in each subfigure, the average of A^* is lower at a higher frequency since the average deformation parameter decreases by increasing the frequency [47]. It is important to note that the minimum projected area of the drop in the steady flow is its initial value when the drop is still undeformed and has a spherical shape; in the oscillatory cases, this minimum value occurs when the direction of the flow changes in each periodic cycle. Also, as expected, the drop at higher Ca deforms more and has a higher projected area. This is why $Ca = 1.67$ is used for visualization here among all the other cases in the present study.

Figure 5 demonstrates the dimensionless total lift coefficient as a function of the dimen-

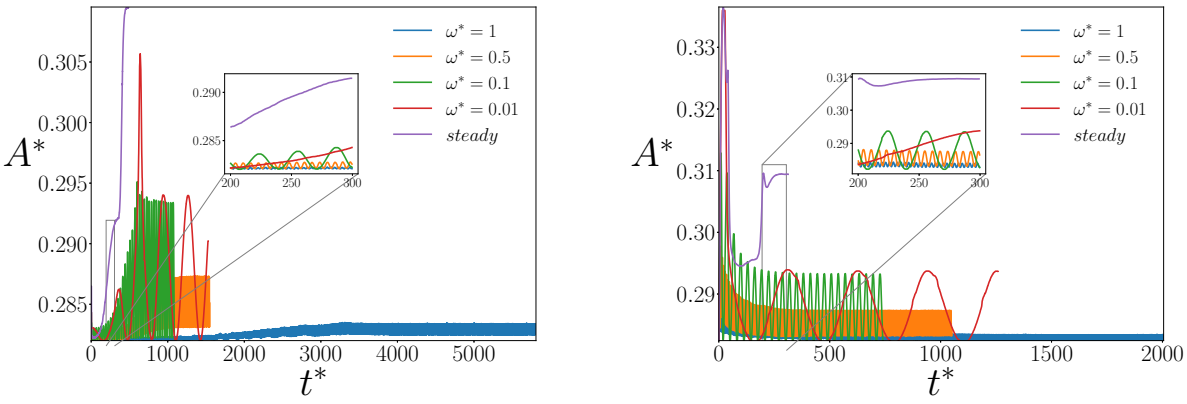

FIG. 4: Transient cross-stream frontal projected area of the drop when it is released from a (a) lower initial location, and an (b) upper initial location

sionless distance of the drop from the channel center in the steady flows and at different Ca. Similar to [18], all of the lift coefficients in this work are obtained by dividing the derived lift force, according to the introduced methodology in the previous section, by a factor of $\frac{\pi}{8}\rho V_{avg,s}^2(2a)^2$, in which $V_{avg,s}$ is the average of flow velocity across the channel cross-section in the steady flow. As expected, we observe that each lift curve has a stable equilibrium point at the corresponding drop focal point. Furthermore, at each Ca, the maximum positive total lift occurs when the drop migration velocity is also maximum. This maximum value is the highest at the lowest Ca. In addition, the maximum negative total lift is at the initial location of the upper trajectory, and its absolute value is the highest for higher Ca except for $Ca = 1.67$. This is because as we go further up from the channel center and the drop focal point, the deformation lift becomes the dominant force. According to equation 13, this force is larger at higher Ca. Also, the negative lift sign in this region is due to the direction of the deformation-induced force, which is toward the center. The drop at $Ca = 1.67$ is released from an initial location closer to the center compared to other cases because it has the highest deformability among all. When it was released from the same location as that of the others, it experienced an extremely large deformation that led to its break up. Therefore, the selected initial point for $Ca = 1.67$ is the furthest possible one from the center that results in the largest possible deformation of the drop throughout its upper trajectory without its break up. Consequently, since the drop in this case starts to travel from a closer distance from the center, it has a lower maximum negative total lift compared to $Ca = 1$ and $Ca = 0.5$ (please refer to eq. 13 that shows the dependence of the

deformation force on the drop distance from the center).

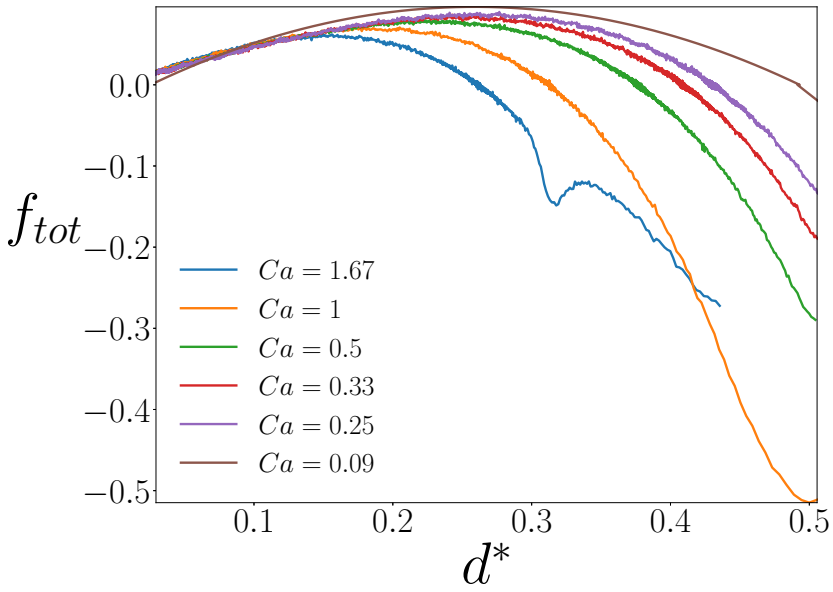

FIG. 5: Total lift coefficient for the steady flows at different Ca

Since the principal hypothesis underlying equation 13 is that the wall effect is negligible due to the large distance of the drop from it [31, 33, 36], we can assume that the shear-gradient force is the dominant component of the inertial lift in our study. After subtracting the calculated deformation lift based on this equation from the obtained total lift (fig. 5), we can derive the inertial lift, as shown in fig. 6. We see that the inertial lift coefficient increases as we increase the Ca number. This could make sense as the more deformed shape of the drop can help further increase the difference between the relative velocities of the fluid with respect to the drop on the channel wall and center sides, which is the chief reason for the shear-gradient force existence [31]. According to eq. 13, the deformation force is a linear function of the drop distance from the center and is larger for higher values of Ca. Because of this trivial conclusion, a plot of this force is not depicted here.

The discussions in the previous two paragraphs are also visible in fig. 7 where the inertial and deformation lifts in the steady flows are plotted against the droplet migration velocity (v^*) in subfigures (a) and (b), respectively, at various Ca. We further note that unlike the linear dependency of the deformation lift on the flow average velocity V_{avg}, this force is a non-linear function of the drop migration velocity. Also, the obtained total force from eq. 8 is orders of magnitude smaller than the calculated drag force in this equation. Therefore, since the term Re_{rel} in eq. 11 is negligible compared to 1, the derived total lift from eq. 8

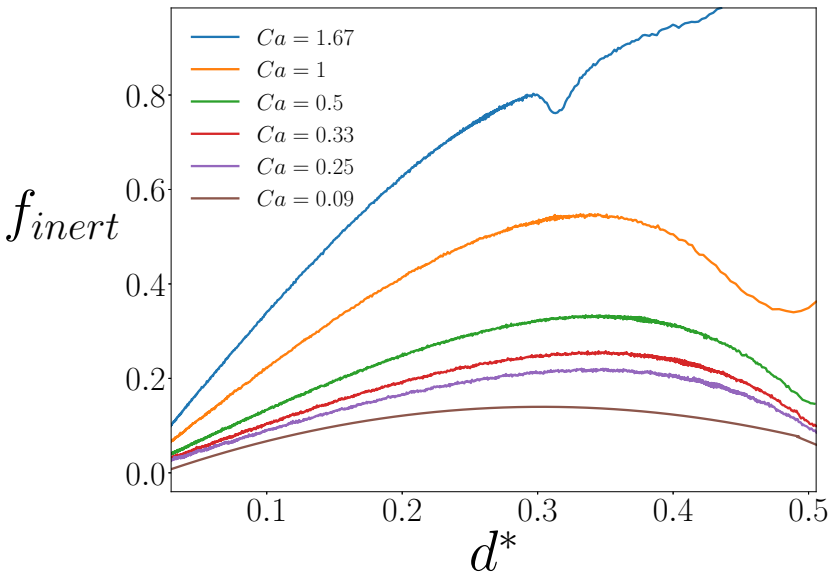

FIG. 6: Inertial lift coefficient for the steady flows at different Ca

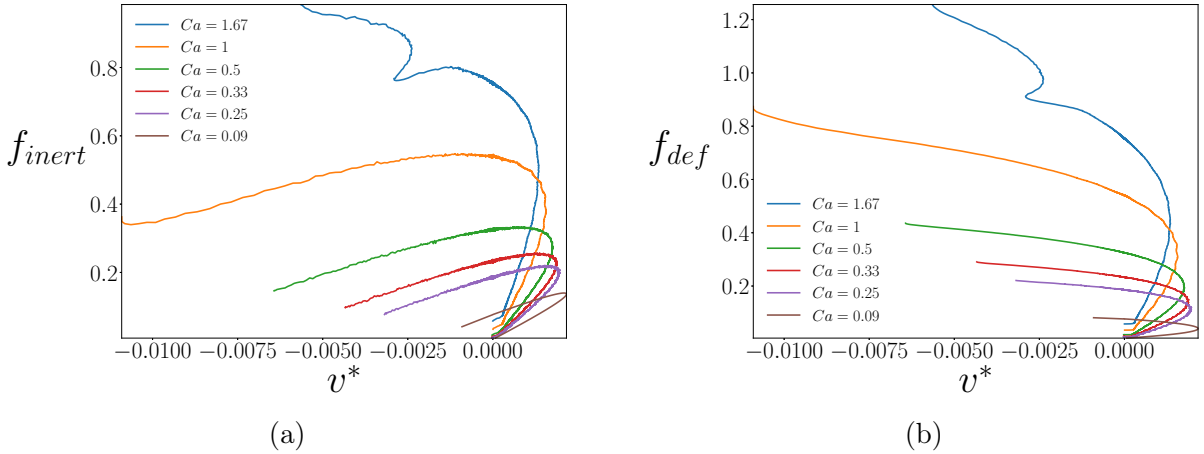

(a) (b)

FIG. 7: The relationships between droplet migration velocity with (a) inertial lift and (b) deformation lift coefficients for the steady flows at different Ca

is approximately a linear function of the drop migration velocity.

Total lift curves acting on the drop in steady and different oscillatory flows at a few Ca numbers are expressed in fig. 8. In each subfigure, the higher the drop migration velocity, the larger are both the amplitude of oscillations and the distance between two corresponding points (e.g. maximum or minimum in the oscillatory cycle) on two consecutive periodic cycles. Hence, similar to steady regimes, the maximum absolute values of oscillatory lift coefficients occur when the drop migration velocities are maximum as well. Similarly, the lift oscillations around the drop focal point and near the lower initial point are lower because

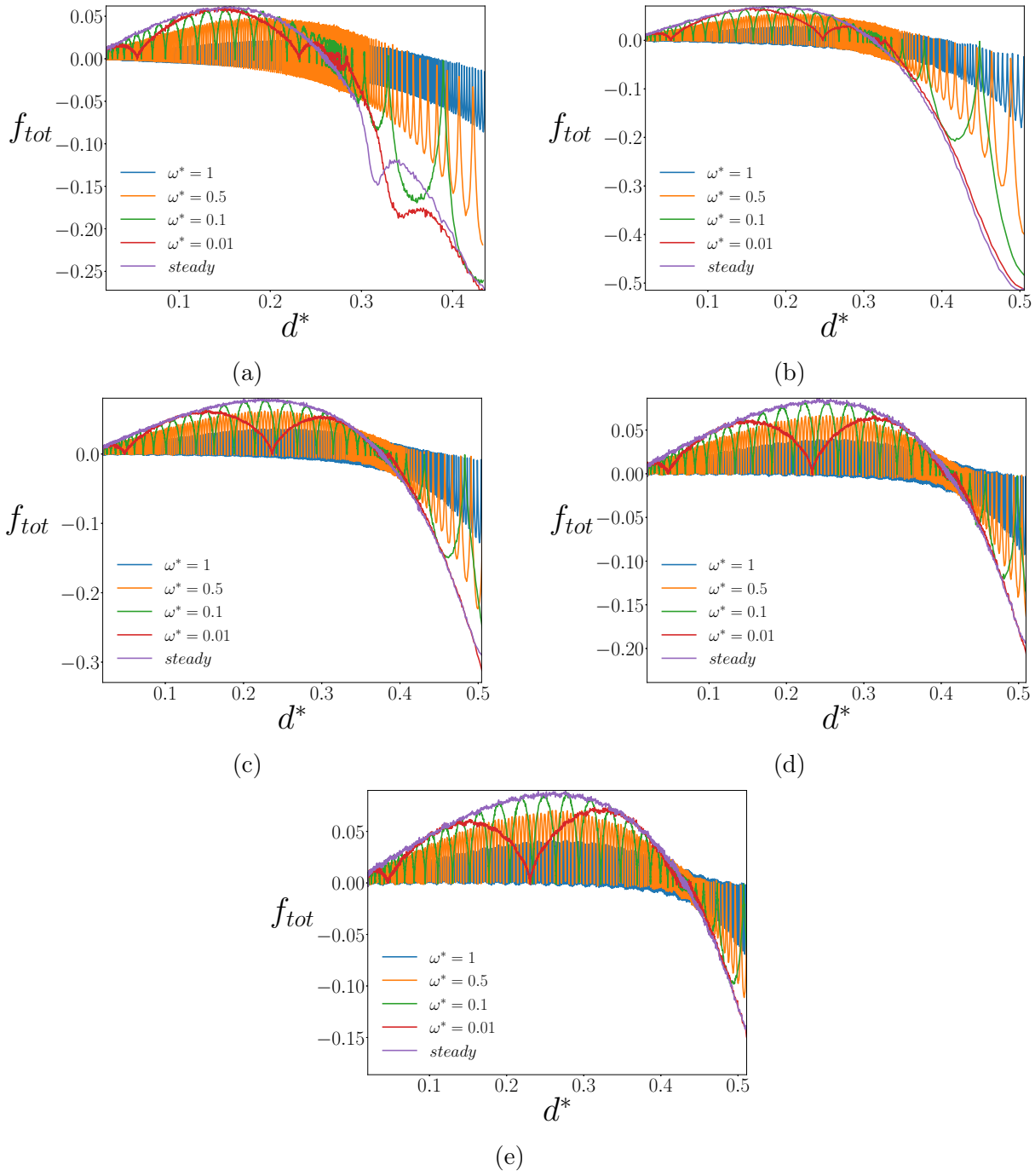

FIG. 8: Total lift coefficients for steady and oscillatory flows with different frequencies at (a) $Ca = 1.67$, (b) $Ca = 1$, (c) $Ca = 0.5$, (d) $Ca = 0.33$, and (e) $Ca = 0.25$

the drop migration velocities are minimum at those locations.

The moving averages of the total lift coefficients in fig. 8 are plotted in fig. 9. The selected d^*_{avg} while computing the average of lift in each corresponding oscillatory cycle is chosen to be the middle value of d^* in that period. Therefore, since oscillatory cycles with

lower frequencies have longer periods, the averaged lift curves at lower frequencies cover a shorter length of d^*_{avg} (a later beginning and a sooner ending). We first note that the obtained averaged lift curves for the oscillatory flows are not necessarily as smooth as that of the steady lift at the corresponding Ca. This observation becomes more pronounced as we increase ω^* or decrease Ca. Nevertheless, these fluctuations on the curves are negligible compared to those of the original oscillatory lifts (fig. 8). Additionally, although the average of inertial and deformation-induced lift forces decrease separately by increasing ω^* [47], the difference between them (fig. 9) does not follow the same pattern. This confirms the existence of a drop focal point with an extremum distance from the channel center at an intermediate frequency, as elaborated in our previous work [47]. Despite this, the average of lift is the largest in the steady flow and the smallest in the oscillatory flow with the highest frequency at each Ca in our study.

By taking another close look at fig. 8, we realize that each of the oscillatory total lift coefficients can be fitted using an expression that comprises of a base curve, which can be best fitted by a 4th order polynomial, combined with the absolute value of some sinusoidal oscillations. Both the amplitude of oscillations and oscillatory periods can be controlled by the drop migration velocity and have direct relationship with it. In other words, the proposed expression can have the following form:

$$f_{tot} \approx \left\{ m + nv(t) \left| cos\left(\frac{c}{av(t)} d(t) + b \right) \right| \right\} \left\{ gd^4(t) + hd^3(t) + kd^2(t) + ld(t) + q \right\} \qquad (18)$$

Where $d(t)$ and $v(t)$ are the time-dependent drop distance from the channel center and its migration velocity, respectively, and m, n, a, b, c, g, h, k, l, and q are the constants to be determined while performing the optimization. The constant m is just placed for achieving higher accuracy for the fits, and it ends up to be almost zero compared to other constants in the expression. The resultant curves are plotted in fig. 10 against their corresponding data (fig. 8a) for $Ca = 1.67$ and $\omega^* = 0.01$, $\omega^* = 0.1$, $\omega^* = 0.5$, and $\omega^* = 1$ with R^2 scores of 0.99, 0.99, 0.98, and 0.93, respectively. Similar curves having the same proposed expression with R^2 scores of 0.93 or higher and capable of capturing all the infinitesimal details are obtained for other Ca numbers as well.

To further extend the total lift prediction to more general cases within a continuous range of Ca and ω^*, we consider the steady and averaged oscillatory lifts (fig. 9) for regression

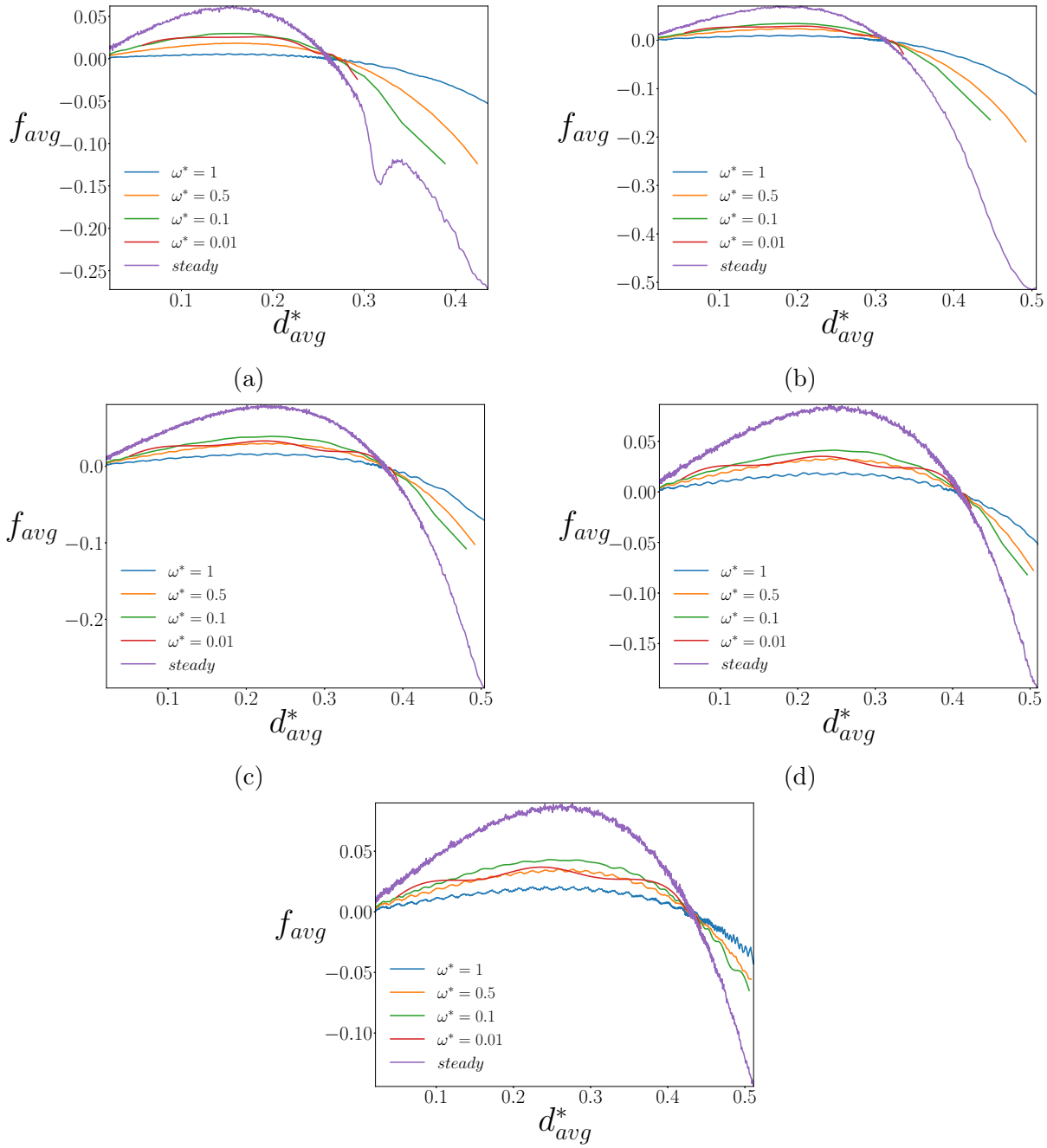

FIG. 9: Averaged total lift coefficients for steady and oscillatory flows with different frequencies at (a) $Ca = 1.67$, (b) $Ca = 1$, (c) $Ca = 0.5$, (d) $Ca = 0.33$, and (e) $Ca = 0.25$

with a 4th order polynomial here. In other words, the expression in the first bracket of eq. 18 is replaced with a value of 1. Using the analytical set of equations 19, we can derive the unknown coefficients a, b, c, g, and h of the polynomial analytically. In these equations, the subscripts for d and f denote their locations. For instance, the subscript max represents

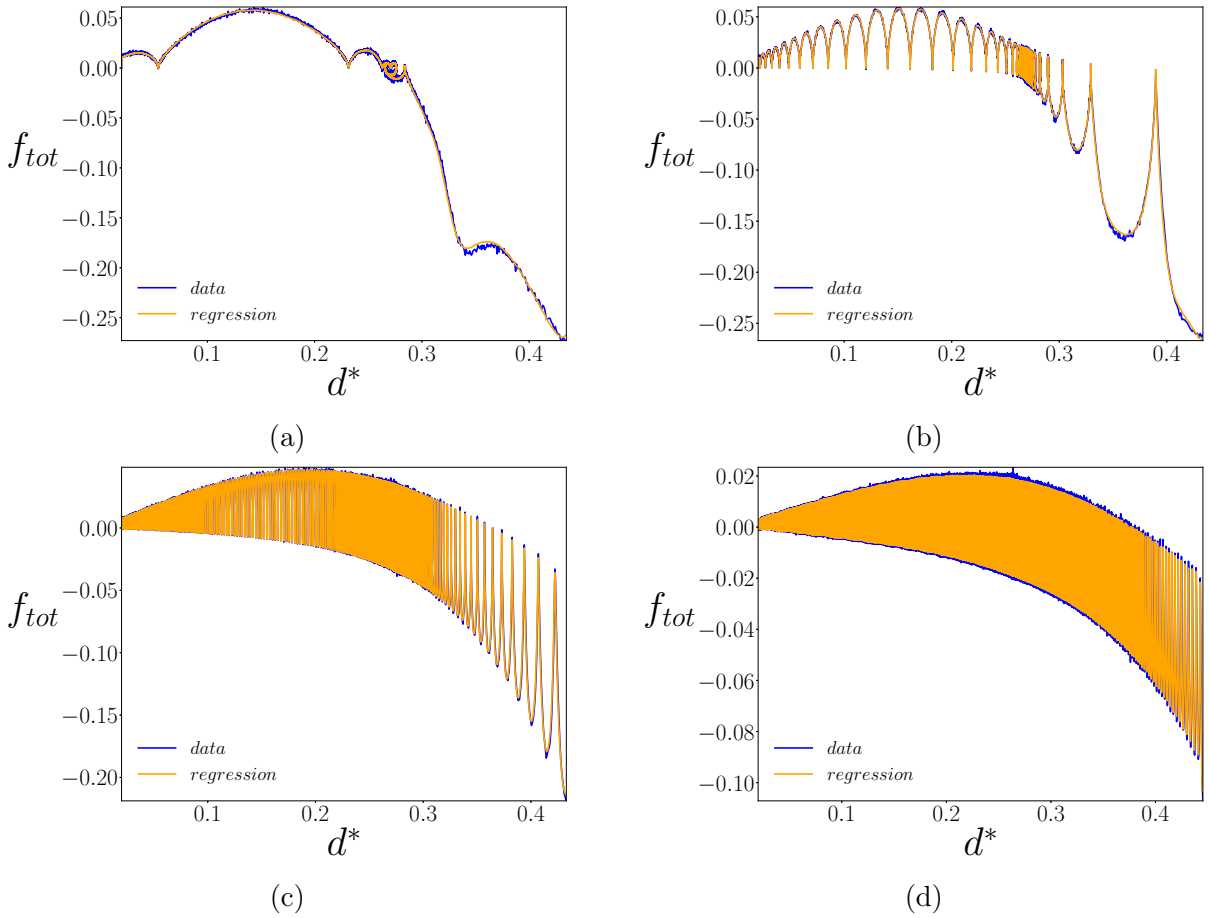

FIG. 10: The fitted total lift coefficients to the ground-truth data using the introduced non-linear regression at $Ca = 1.67$ and (a) $\omega^* = 0.01$, (b) $\omega^* = 0.1$, (c) $\omega^* = 0.5$, and (d) $\omega^* = 1$

where the magnitude of total (or averaged) lift is maximum and its first derivative is zero. The obtained polynomials with this approach have R^2 scores of around 0.9 or higher for the cases presented in fig. 9.

$$\begin{cases} ad_{first}^4 + bd_{first}^3 + cd_{first}^2 + gd_{first} + h = f_{first}, \\ ad_{max}^4 + bd_{max}^3 + cd_{max}^2 + gd_{max} + h = f_{max}, \\ 4ad_{max}^3 + 3bd_{max}^2 + 2cd_{max} + g = 0, \\ ad_{eq}^4 + bd_{eq}^3 + cd_{eq}^2 + gd_{eq} + h = 0, \\ ad_{last}^4 + bd_{last}^3 + cd_{last}^2 + gd_{last} + h = f_{last}, \end{cases} \tag{19}$$

Parameters d_{first}, d_{max}, d_{eq}, d_{last}, f_{first}, f_{max}, and f_{last} are already available for the cases

in fig. 9 to solve the system of equations 19 for them. However, we use the multi-fidelity Gaussian processes (MFGP) method to predict these unknown parameters for any given double inputs of $0.25 \leq Ca \leq 1.67$ and $0 \leq \omega^* \leq 1$. MFGP is a Bayesian stochastic approach that does a casual inference on a set of high and low-fidelity datasets, and it is extremely effective if there are strong correlations between them [59]. This method is described in detail in our previous work, and it is carried out to predict the distance of the drop equilibrium position from the channel center (d_{eq}) with R^2 of 0.99 and root mean squared error (RMSE) of 0.01 in that work [47]. Here, we refer to the data for the cases in fig. 9 except for $Ca = 1$ as our high-fidelity data. We generate similar data for all the cases in that figure, but with a grid of $128 \times 76 \times 76$ in the x, y, and z directions, respectively, and having 13038 triangular elements for the discretization of the drop. We consider this data as our low-fidelity dataset. Therefore, we have a total of 25 low and 20 high-fidelity data points, which satisfies the required nested structure to apply MFGP on the data [59]. We randomly allocate 5 data points of the entire high-fidelity dataset as our test set since the high-fidelity response is our main target. We train the algorithm on the remaining 40 training data points and evaluate its performance on the test set. We repeat this procedure 30 times and compute the average of evaluation metrics so that the selection of test sets does not significantly affect the overall algorithm performance.

Table I presents the average of R^2 and RMSE on our 6 remaining unknown parameters after completing the aforementioned steps. We can see that the trained algorithm is capable of predicting the intended parameters with very high accuracies. Especially, the accurate prediction of f_{max} and f_{last} is useful for determining the maximum and minimum values of averaged total lift for any given input in the range, respectively. The slightly less accurate prediction for d_{max} (i.e. where the maximum averaged lift occurs) is because of the present randomness in its values among different cases. This is unlike the consistent pattern that exists for other parameters for a combination of ω^* values across different Ca numbers. The similar lower accurate prediction for d_{last} is due to the lack of data points between $Ca = 1$ and $Ca = 1.67$ since all the cases with $Ca \leq 1$ have the same upper release initial location. However, the R^2 score of around 0.8 for this prediction is still high, and it can help us determine the furthest starting point from the center and the widest traveling region of a droplet with $1 \leq Ca \leq 1.67$ in the microchannel so that it undergoes the largest possible deformation without breaking up.

Parameter	R^2	RMSE
d_{max}	0.83	0.0138
d_{last}	0.78	0.0219
d_{first}	0.97	0.0008
f_{last}	0.93	0.0170
f_{max}	0.98	0.0017
f_{first}	0.97	0.0005

TABLE I: MFGP averaged performance metrics on 30 randomly chosen test sets for the parameters required for the determination of the analytical averaged total lift polynomial coefficients

IV. CONCLUSIONS

The dynamics of particles and biological cells in microchannels has caught many researchers' attention because of several biomicrofluidic applications it has. The underlying physics owes its behavior mainly to the presence of different lift forces in such channels. Hence, many scientists have dedicated their time to calculate or measure these forces. However, most of these works have focused on analyzing the lift forces acting on solid and non-deformable particles and studied the effects of parameters such as particles' size, Reynolds number, etc on them. Consequently, such analysis on deformable droplets or bubbles and studying the effects of varying parameters like Capillary number is almost missing in the literature. In this work, we have extended such analysis to the case of a single deformable droplet in the channel. We have calculated the main components of the lift force based on a unique methodology that merely depends on the drop trajectory. To do so, first, the drop migration velocity and its frontal projected area as it travels its lateral trajectory have been computed to calculate the drag force in the wall-normal direction accurately. After applying Newton's second law on the drop, the total lift profile is obtained over a region where the drop has a distance higher than its diameter from the wall. It has been observed that the total lift has a higher maximum at a lower Capillary, and its minimum decreases as we increase the Ca. The inertial and deformation-induced lift forces both increase by increasing the Ca number. Moreover, since the oscillatory flows within the microchannel were previously shown to enable working with sub-micron biological particles as well as introducing new focal points for them, we have also included these flow regimes in our analysis and investigated the effects of oscillation frequency on the lift in addition to the Capillary number. We have seen that for all cases, the total lift and for oscillatory ones, the ampli-

tude of oscillations are both higher when the drop migration velocity is higher. At each Ca, the steady lift and moving averages of oscillatory ones at different ω^* have also been compared. It has been shown that the steady lift has the largest magnitude, and the average of oscillatory one with the highest frequency in this study has the smallest strength. However, there is not a constant decreasing pattern in the average of lift by increasing the frequency, which is why the drop focuses furthest from the channel center at an intermediate ω^*. Additionally, an accurate mathematical expression has been proposed that captures the detailed total oscillatory lift curves at various ω^* with R^2 scores of 0.97 or higher. Finally, the multi-fidelity Gaussian processes has been used to accurately predict the 7 unknown parameters required to define a simple 4th order polynomial to fit the steady and averaged oscillatory lifts with R^2 scores of about 0.9 or higher for any given Ca and ω^* within the ranges of $0.25 \leq Ca \leq 1.67$ and $0 \leq \omega^* \leq 1$.

V. CONFLICTS OF INTEREST

There are no conflicts of interest to declare.

VI. ACKNOWLEDGEMENT

This work is supported by the National Science Foundation (Grant No. CBET-1705371) and by the USDA National Institute of Food and Agriculture (Hatch project 1017342).

[1] Gossett DR, Weaver WM, Mach AJ, Hur SC, Tse HTK, Lee W, et al. Label-free cell separation and sorting in microfluidic systems. Analytical and bioanalytical chemistry. 2010;397(8):3249-67.

[2] Toner M, Irimia D. Blood-on-a-chip. Annu Rev Biomed Eng. 2005;7:77-103.

[3] Gossett DR, Henry T, Lee SA, Ying Y, Lindgren AG, Yang OO, et al. Hydrodynamic stretching of single cells for large population mechanical phenotyping. Proceedings of the National Academy of Sciences. 2012;109(20):7630-5.

[4] Karimi A, Yazdi S, Ardekani A. Hydrodynamic mechanisms of cell and particle trapping in microfluidics. Biomicrofluidics. 2013;7(2):021501.

[5] Di Carlo D. Inertial microfluidics. Lab on a Chip. 2009;9(21):3038-46.

[6] Martel JM, Toner M. Inertial focusing in microfluidics. Annual review of biomedical engineering. 2014;16:371-96.

[7] Bazaz SR, Mashhadian A, Ehsani A, Saha SC, Krüger T, Warkiani ME. Computational inertial microfluidics: a review. Lab on a Chip. 2020;20(6):1023-48.

[8] Connolly S, Newport D, McGourty K. The mechanical responses of advecting cells in confined flow. Biomicrofluidics. 2020;14(3):031501.

[9] Stoecklein D, Di Carlo D. Nonlinear microfluidics. Analytical chemistry. 2018;91(1):296-314.

[10] Di Carlo D, Edd JF, Humphry KJ, Stone HA, Toner M. Particle segregation and dynamics in confined flows. Physical review letters. 2009;102(9):094503.

[11] Prohm C, Stark H. Feedback control of inertial microfluidics using axial control forces. Lab on a Chip. 2014;14(12):2115-23.

[12] Su J, Chen X, Zhu Y, Hu G. Machine learning assisted fast prediction of inertial lift in microchannels. Lab on a Chip. 2021.

[13] Wang Q, Yuan D, Li W. Analysis of hydrodynamic mechanism on particles focusing in microchannel flows. Micromachines. 2017;8(7):197.

[14] Asmolov ES, Dubov AL, Nizkaya TV, Harting J, Vinogradova OI. Inertial focusing of finite-size particles in microchannels. Journal of Fluid Mechanics. 2018;840:613-30.

[15] Liu C, Xue C, Sun J, Hu G. A generalized formula for inertial lift on a sphere in microchannels. Lab on a Chip. 2016;16(5):884-92.

[16] Zastawny M, Mallouppas G, Zhao F, Van Wachem B. Derivation of drag and lift force and torque coefficients for non-spherical particles in flows. International Journal of Multiphase Flow. 2012;39:227-39.

[17] Mannan FO, Leiderman K. Weak inertial effects on arbitrarily shaped objects in the presence of a wall. Physical Review Fluids. 2020;5(4):044102.

[18] Chen X, Xue C, Zhang L, Hu G, Jiang X, Sun J. Inertial migration of deformable droplets in a microchannel. Physics of Fluids. 2014;26(11):112003.

[19] Rivero-Rodriguez J, Scheid B. Bubble dynamics in microchannels: inertial and capillary migration forces–CORRIGENDUM. Journal of Fluid Mechanics. 2018;855:1242-5.

[20] Stan CA, Guglielmini L, Ellerbee AK, Caviezel D, Stone HA, Whitesides GM. Sheathless hydrodynamic positioning of buoyant drops and bubbles inside microchannels. Physical Review

E. 2011;84(3):036302.

[21] Zhou J, Papautsky I. Fundamentals of inertial focusing in microchannels. Lab on a Chip. 2013;13(6):1121-32.

[22] Raffiee AH, Ardekani AM, Dabiri S. Numerical investigation of elasto-inertial particle focusing patterns in viscoelastic microfluidic devices. Journal of Non-Newtonian Fluid Mechanics. 2019;272:104166.

[23] Schaaf C, Stark H. Inertial migration and axial control of deformable capsules. Soft Matter. 2017;13(19):3544-55.

[24] Mutlu BR, Edd JF, Toner M. Oscillatory inertial focusing in infinite microchannels. Proceedings of the National Academy of Sciences. 2018;115(30):7682-7.

[25] Lafzi A, Raffiee AH, Dabiri S. Inertial migration of a deformable capsule in an oscillatory flow in a microchannel. Physical Review E. 2020;102(6):063110.

[26] Schonewill PP. Oscillatory flow: Effect on transverse diffusivity and inertial migration of particles and bubbles. University of Notre Dame; 2008.

[27] Unverdi SO, Tryggvason G. A front-tracking method for viscous, incompressible, multi-fluid flows. Journal of computational physics. 1992;100(1):25-37.

[28] Maxey MR, Riley JJ. Equation of motion for a small rigid sphere in a nonuniform flow. The Physics of Fluids. 1983;26(4):883-9.

[29] Zenit R, Legendre D. The coefficient of restitution for air bubbles colliding against solid walls in viscous liquids. Physics of Fluids. 2009;21(8):083306.

[30] Jeong H, Park H. Near-wall rising behaviour of a deformable bubble at high Reynolds number. Journal of Fluid Mechanics. 2015;771:564-94.

[31] Zhang J, Yan S, Yuan D, Alici G, Nguyen NT, Warkiani ME, et al. Fundamentals and applications of inertial microfluidics: a review. Lab on a Chip. 2016;16(1):10-34.

[32] Seo KW, Kang YJ, Lee SJ. Lateral migration and focusing of microspheres in a microchannel flow of viscoelastic fluids. Physics of Fluids. 2014;26(6):063301.

[33] Ho B, Leal L. Inertial migration of rigid spheres in two-dimensional unidirectional flows. Journal of fluid mechanics. 1974;65(2):365-400.

[34] Bagchi P, Balachandar S. Shear versus vortex-induced lift force on a rigid sphere at moderate Re. Journal of Fluid Mechanics. 2002;473:379-88.

[35] Fay ME, Myers DR, Kumar A, Turbyfield CT, Byler R, Crawford K, et al. Cellular softening mediates leukocyte demargination and trafficking, thereby increasing clinical blood counts. Proceedings of the National Academy of Sciences. 2016;113(8):1987-92.

[36] Jahromi S, Amani E, Movahed S. An improved hybrid continuum-atomistic four-way coupled model for electrokinetics in nanofluidics. Electrophoresis. 2019;40(12-13):1678-90.

[37] Ishii M, Zuber N. Drag coefficient and relative velocity in bubbly, droplet or particulate flows. AIChE journal. 1979;25(5):843-55.

[38] Snyder MR, Knio OM, Katz J, Le Maître OP. Statistical analysis of small bubble dynamics in isotropic turbulence. Physics of Fluids. 2007;19(6):065108.

[39] Zhou Y, Zhao C, Bo H. Analyses and modified models for bubble shape and drag coefficient covering a wide range of working conditions. International Journal of Multiphase Flow. 2020;127:103265.

[40] Kelbaliyev G, Ceylan K. Development of new empirical equations for estimation of drag coefficient, shape deformation, and rising velocity of gas bubbles or liquid drops. Chemical Engineering Communications. 2007;194(12):1623-37.

[41] Salibindla AK, Masuk AUM, Tan S, Ni R. Lift and drag coefficients of deformable bubbles in intense turbulence determined from bubble rise velocity. Journal of Fluid Mechanics. 2020;894.

[42] Ceylan K, Altunbaş A, Kelbaliyev G. A new model for estimation of drag force in the flow of Newtonian fluids around rigid or deformable particles. Powder technology. 2001;119(2-3):250-6.

[43] Shao C, Luo K, Fan J. Detailed numerical simulation of unsteady drag coefficient of deformable droplet. Chemical Engineering Journal. 2017;308:619-31.

[44] Aggarwal S, Peng F. A review of droplet dynamics and vaporization modeling for engineering calculations. J Eng Gas Turbines Power. 1995;117(3):453-61.

[45] Chan PH, Leal L. The motion of a deformable drop in a second-order fluid. Journal of Fluid Mechanics. 1979;92(1):131-70.

[46] Stan CA, Ellerbee AK, Guglielmini L, Stone HA, Whitesides GM. The magnitude of lift forces acting on drops and bubbles in liquids flowing inside microchannels. Lab on a Chip. 2013;13(3):365-76.

[47] Lafzi A, Dabiri S. Dynamics of droplet migration in oscillatory and pulsating microchannel flows and prediction and uncertainty quantification of its lateral equilibrium position using multifidelity Gaussian processes. Physics of Fluids. 2021;33(6):062010.

[48] Pan Dy, Lin Yq, Zhang Lx, Shao Xm. Motion and deformation of immiscible droplet in plane Poiseuille flow at low Reynolds number. Journal of Hydrodynamics. 2016;28(4):702-8.

[49] Lan H, Khismatullin DB. A numerical study of the lateral migration and deformation of drops and leukocytes in a rectangular microchannel. International journal of multiphase flow. 2012;47:73-84.

[50] Chaudhury K, Mandal S, Chakraborty S. Droplet migration characteristics in confined oscillatory microflows. Physical Review E. 2016;93(2):023106.

[51] Razi M, Pourghasemi M. Direct numerical simulation of deformable droplets motion with uncertain physical properties in macro and micro channels. Computers & Fluids. 2017;154:200-10.

[52] Sundqvist H, Veronis G. A simple finite-difference grid with non-constant intervals. Tellus. 1970;22(1):26-31.

[53] Salibindla AK, Masuk AUM, Ni R. Experimental investigation of the acceleration statistics and added-mass force of deformable bubbles in intense turbulence. Journal of Fluid Mechanics. 2021;912.

[54] Sangani AS, Zhang D, Prosperetti A. The added mass, Basset, and viscous drag coefficients in nondilute bubbly liquids undergoing small-amplitude oscillatory motion. Physics of Fluids A: Fluid Dynamics. 1991;3(12):2955-70.

[55] Presas A, Luo Y, Wang Z, Guo B. Fatigue life estimation of Francis turbines based on experimental strain measurements: Review of the actual data and future trends. Renewable and Sustainable Energy Reviews. 2019;102:96-110.

[56] Dincau B, Dressaire E, Sauret A. Pulsatile Flow in Microfluidic Systems. Small. 2020;16(9):1904032.

[57] Aggarwal N, Sarkar K. Deformation and breakup of a viscoelastic drop in a Newtonian matrix under steady shear. Journal of Fluid Mechanics. 2007;584:1-21.

[58] Marson RL, Huang Y, Huang M, Fu T, Larson RG. Inertio-capillary cross-streamline drift of droplets in Poiseuille flow using dissipative particle dynamics simulations. Soft matter. 2018;14(12):2267-80.

[59] Perdikaris P, Raissi M, Damianou A, Lawrence N, Karniadakis GE. Nonlinear information fusion algorithms for data-efficient multi-fidelity modelling. Proceedings of the Royal Society A: Mathematical, Physical and Engineering Sciences. 2017;473(2198):20160751.